Ideal incompressible axisymmetric MHD: Uncovering finite-time singularities

Sai Swetha Venkata Kolluru* and Rahul Pandit†
Centre for Condensed Matter Theory, Department of Physics, Indian Institute of Science, Bengaluru 560012, India

(Received 28 September 2025; accepted 14 May 2026; published 10 June 2026)

We provide compelling numerical evidence for the development of (potential) finite-time singularities in the three-dimensional axisymmetric, ideal, incompressible magnetohydrodynamic (IMHD) equations, in a wall-bounded cylindrical domain, starting from smooth initial data, for the velocity and magnetic fields. We demonstrate that the nature of the singularity depends crucially on the relative strength $\mathcal{C}$ of the velocity and magnetic fields at the time of initialization: (i) if $\mathcal{C} < 1$, then the swirl components, at the wall, evolve toward square profiles that lead to the intensification of shear at the meridional plane $(r = 1, z = L/2)$ and the development of a finite-time singularity; (ii) if $\mathcal{C} = 1$, there is no temporal evolution; (iii) if $\mathcal{C} > 1$, then the swirl components, at the wall, evolve toward a cusp-type singularity. By examining the spatiotemporal evolution of the pressure, we obtain insights into the development of these singularities.

DOI: 10.1103/l645-3ljm

I. INTRODUCTION

Among the many interesting problems posed by the partial differential equations (PDEs) of fluid dynamics, perhaps the most challenging is proving the global regularity of their solutions. For the three-dimensional (3D) Navier–Stokes equation (NSE), which governs the motion of a Newtonian fluid [1–6], the global-regularity problem is one of the Clay Millennium Prize problems [7,8]. A proof of global regularity (or lack thereof) should show that, starting with smooth initial data for the hydrodynamical fields, solutions of the PDE do not develop (or develop) singularities in finite time. For the two-dimensional (2D) NSE and Euler equation, global regularity has been proved for analytic initial data [9]. By contrast, the proofs of the global regularity of solutions of the 3D NSE and its inviscid forerunner, the 3D Euler equation, continue to be open problems. Furthermore, the breakdown of the regularity of solutions of the 3D Euler equation has been conjectured to be important for understanding anomalous dissipation for turbulent solutions of the 3D NSE, in the limit of vanishing viscosity [10,11].

The global-regularity problem remains open in both 2D and 3D [12], even for the ideal, incompressible MHD (IMHD) equations, which govern the dynamics of an incompressible, inviscid conducting fluid with zero magnetic diffusivity and are of relevance in astrophysics, space physics, geophysics, nuclear fusion, and liquid-metal flows [13–20]. The existence (or nonexistence) of a finite-time singularity (FTS) in the solutions of the IMHD equations is of importance not only from a mathematical standpoint, but also from the point of view of physics [21]. Numerical studies of 3D incompressible MHD turbulence have shown that, at high Reynolds numbers and high magnetic Reynolds numbers, the rate of total energy dissipation reaches a positive constant value [22–24]; this phenomenon is reminiscent of anomalous dissipation at high Reynolds numbers in 3D NS

*Contact author: venkata-saiswetha.kolluru@cea.fr
†Contact author: rahul@iisc.ac.in

turbulence. Consequently, it has been conjectured that the breakdown of global regularity for the 3D IMHD equations might be related to anomalous dissipation in MHD turbulence [25].

Numerical investigations of both the 3D incompressible Euler [26,27] and the 3D IMHD equations [21,28,29], in spatially periodic domains, have not yielded conclusive evidence for or against an FTS. By contrast, there is growing numerical evidence for a potential FTS in the 3D-axisymmetric incompressible Euler (3DAE) equations, in a wall-bounded cylindrical domain. This was first reported in the adaptive-mesh calculation of Ref. [30], which reported the development of a ringlike singularity on the wall of the cylinder in the meridional plane at an estimated singularity time $t_* \simeq 0.003\,505\,6$. This potential FTS was reexamined and confirmed using Fourier–Chebyshev pseudospectral [31,32] and Cauchy–Lagrange [33] methods. The role of pressure in the development of this FTS was elucidated in Ref. [31].

In this paper we provide compelling numerical evidence for a similar FTS for the 3D-axisymmetric IMHD equations in a wall-bounded domain, with smooth initial data for both velocity and magnetic fields (akin to the initial condition in Refs. [30,32] for the 3DAE). Furthermore, we uncover a new type of FTS by tuning the ratio $\mathcal{C}$ of the magnitudes of the initial magnetic and velocity fields. If $\mathcal{C} < 1$, the evolution of the FTS is akin to that in the 3DAE [30,32,33]. In contrast, if $\mathcal{C} > 1$, then the swirl components of the fields develop cusplike structures at the wall that lead, in turn, to a potential FTS. This novel cusp-type singularity has not been seen for any axisymmetric hydrodynamical partial differential equation [34]. For both cases $\mathcal{C} < 1$ and $\mathcal{C} > 1$, the vorticity and current fields show rapid growth.

II. MODEL

The evolution of an incompressible, inviscid, perfectly conducting fluid is governed by the incompressible, ideal MHD equations (IMHD) below:

$$\partial_t \boldsymbol{u} + \boldsymbol{u}\cdot\nabla\boldsymbol{u} = -\nabla p + \boldsymbol{j}\times\boldsymbol{b}; \tag{1a}$$

$$\partial_t \boldsymbol{b} = \nabla\times(\boldsymbol{u}\times\boldsymbol{b}). \tag{1b}$$

In cylindrical coordinates, the velocity field is written as

$$\boldsymbol{u}(r,z,t) = (u^r(r,z,t), u^\theta(r,z,t), u^z(r,z,t)).$$

Here, $\nabla\cdot\boldsymbol{u} = 0$ and $\nabla\cdot\boldsymbol{b} = 0$; there is a similar expression for the magnetic field $\boldsymbol{b}$; and the superscripts r, θ, and z denote the radial, swirl, and axial components of the fields.

The pressure field p in the IMHD equations (1) can be eliminated using the vorticity $\boldsymbol{\omega} = \nabla\times\boldsymbol{u}$ and the current density $\boldsymbol{j} = \nabla\times\boldsymbol{b}$, and we can rewrite the above equations in the following vorticity and current formulation:

$$\partial_t\boldsymbol{\omega} = \nabla\times(\boldsymbol{u}\times\boldsymbol{\omega}) + \nabla\times(\boldsymbol{j}\times\boldsymbol{b}); \tag{2}$$

$$\partial_t\boldsymbol{j} = \nabla\times(\nabla\times(\boldsymbol{u}\times\boldsymbol{b})). \tag{3}$$

In 3D, the stream function $\boldsymbol{\psi}$ and magnetic potential $\boldsymbol{\phi}$ are vector quantities that are related to the primitive variables in Eqs. (1a)–(3) via $\boldsymbol{u} = \nabla\times\boldsymbol{\psi}$ and $\boldsymbol{b} = \nabla\times\boldsymbol{\phi}$. We represent vector fields in the 3D-axisymmetric domain as follows: $\boldsymbol{u}(r,z,t) = u^r(r,z,t)\,\hat{e}_r + u^\theta(r,z,t)\,\hat{e}_\theta + u^z(r,z,t)\,\hat{e}_z$, where $\hat{e}_r$, $\hat{e}_\theta$, and $\hat{e}_z$ are the basis vectors in the cylindrical coordinate system. We introduce the transformed variables [30,32]

$$u^1 \equiv \frac{u^\theta}{r}, \quad \omega^1 \equiv \frac{\omega^\theta}{r}, \quad b^1 \equiv \frac{b^\theta}{r}, \quad \text{and} \quad j^1 \equiv \frac{j^\theta}{r}, \tag{4}$$

and we rewrite Eq. (1) as follows:

$$\partial_t u^1 = (b^r\partial_r + b^z\partial_z)b^1 - (u^r\partial_r + u^z\partial_z)u^1 - 2(b^1\partial_z\phi^1 - u^1\partial_z\psi^1); \tag{5a}$$

$$\partial_t\omega^1 = (b^r\partial_r + b^z\partial_z)j^1 - (u^r\partial_r + u^z\partial_z)\omega^1 + \partial_z((u^1)^2 - (b^1)^2); \tag{5b}$$

$$\partial_t b^1 = (b^r\partial_r + b^z\partial_z)u^1 - (u^r\partial_r + u^z\partial_z)b^1\,; \tag{5c}$$

$$\begin{aligned}\partial_t j^1 = &-\big(j^1 + 2\partial_z^2\phi^1\big)(2\partial_r u^r - \partial_z\psi^1) + \big(\omega^1 + 2\partial_z^2\psi^1\big)(2\partial_r b^r - \partial_z\phi^1)\\ &+ (b^r\partial_r + b^z\partial_z)\omega^1 - (u^r\partial_r + u^z\partial_z)j^1 - b^1\partial_z u^1 + u^1\partial_z b^1.\end{aligned} \tag{5d}$$

The Poisson equations for ψ^1 and ϕ^1 are given below:

$$\left(\partial_r^2 + \frac{3}{r}\partial_r + \partial_z^2\right)\psi^1 = -\omega^1\,; \tag{6a}$$

$$\left(\partial_r^2 + \frac{3}{r}\partial_r + \partial_z^2\right)\phi^1 = -j^1. \tag{6b}$$

The radial and axial components of the $\boldsymbol{u}$ and $\boldsymbol{b}$ fields are obtained from $\boldsymbol{\psi}$ and $\boldsymbol{\phi}$, respectively:

$$u^r = -r\partial_z\psi^1\,; \quad u^z = 2\psi^1 + r\partial_r\psi^1\,; \tag{7a}$$

$$b^r = -r\partial_z\phi^1\,; \quad b^z = 2\phi^1 + r\partial_r\phi^1. \tag{7b}$$

The solution of the above equations, in terms of the transformed variables $\{u^1, \omega^1, ...\}$ [see Eq. (4)], ensures that the corresponding fields $\{u^\theta, \omega^\theta, ...\}$ remain smooth at the coordinate singularity on the axis of the cylinder ($r = 0$).

We solve the IMHD equations in an axisymmetric cylindrical domain: (i) in the z direction, we use periodic boundary conditions for all fields, and in the r direction, we impose the no-flow condition for $\boldsymbol{u}$, and the perfectly conducting condition for $\boldsymbol{b}$, at the wall, i.e., $u_r(r=1,z,t) = b_r(r=1,z,t) = 0$; (ii) at the axis we use the pole conditions for all fields, namely, that their radial derivatives vanish at $r = 0$ [32,35]:

$$u^r(r=1,z,t) = 0 \Rightarrow \psi^1(r=1,z,t) = 0\,; \tag{8a}$$

$$b^r(r=1,z,t) = 0 \Rightarrow \phi^1(r=1,z,t) = 0\,; \tag{8b}$$

$$\partial_r\psi^1(r=0,z,t) = 0\,; \tag{8c}$$

$$\partial_r\phi^1(r=0,z,t) = 0. \tag{8d}$$

We initialize the velocity field with $u^\theta(r,z,t=0)/r = 100e^{-30(1-r^2)^4}\sin\left(\frac{2\pi}{L}z\right)$ as in Refs. [30,32], and the initial magnetic field $b^\theta(r,z,t=0) = \mathcal{C}u^\theta(r,z,t=0)$ is chosen to be a multiple of the initial velocity where $\mathcal{C}$ controls the strength of b^θ relative to u^θ, at the initial time:

$$u^1(r,z,t=0) = 100e^{-30(1-r^2)^4}\sin\left(\frac{2\pi}{L}z\right), \tag{9}$$

$$b_1(r,z) = Ce^{-(1-r^2)^4}\sin\left(\frac{2\pi z}{L_z}\right). \tag{10}$$

We obtain the pressure p by taking divergence of Eq. (1a), which yields the following Poisson-type equation:

$$\nabla^2\left(p + \frac{|\boldsymbol{b}|^2}{2}\right) = -\nabla\cdot[(\boldsymbol{u}\cdot\nabla)\boldsymbol{u}] + \nabla\cdot[(\boldsymbol{b}\cdot\nabla)\boldsymbol{b}], \tag{11a}$$

$$\partial_r\left(p + \frac{1}{2}|\boldsymbol{b}|^2\right) = ((u^\theta)^2 - (b^\theta)^2), \quad \text{at } r = 1, \forall(z,t). \tag{11b}$$

III. METHODS

We use Fourier–Chebyshev pseudospectral methods to solve Eqs. (5). The domain $\mathcal{D}(1, L)$ is discretized using the collocation grid $\mathbf{X}_{N,M} := \{(r_i, z_j) : i = 0, 1, ..., N-1 \text{ and } j = 0, 1, ..., M-1\}$. In the periodic z direction, the collocation points $\{z_j = \frac{Lj}{M} : j = 0, 1...M-1\}$ are distributed uniformly. In the wall-bounded r direction, the collocation nodes $\{r_i = \frac{1}{2}(1+\cos(\frac{\pi(i-0.5)}{N}) : i = 0, 1, ...N-1\}$ are the roots of $T_N(2r-1)$, the order-N Chebyshev polynomial of the first kind; these roots are spaced nonuniformly, and they cluster near $r = 0$ and $r = 1$. Given function $f(r, z)$, the Fourier–Chebyshev approximation on the grid $\mathbf{X}_{N,M}$ is

$$P_{N,M}f(r,z) = \sum_{|k|\leqslant M/2} \sum_{l=0}^{M-1} \hat{f}(k,l)e^{ikz}\, T_l(2r-1). \tag{12}$$

If $N = M$, the spacing between Chebyshev nodes, near $r = 1$ and $r = 0$, is much smaller than the spacing between the Fourier nodes. Therefore, we use $M > N$; specifically, in our direct numerical simulation (DNS), we use $N = 256$ and $M = 512$, which suffice to uncover the FTSs we explore and the associated tyger oscillations. We use a fourth-order Runge–Kutta scheme, with an adaptive time step that ensures Courant–Friedrichs–Lewy (CFL) stability in both the Fourier-discretized z direction and the Chebyshev-discretized r direction. We compute the derivatives in spectral space and, subsequently, the nonlinear terms in physical space. In order to remove aliasing errors, in both Fourier and Chebyshev spectral approximations, we use the 2/3-dealiazing method [36]. We use our Tau solver [32] to solve the Poisson equations for the swirl components of the stream-function (6a) and magnetic vector potential (6b) with the boundary conditions (8). We also use the Tau solver for solving the pressure-Poisson problem in Eq. (11).

A. Singularity-detection criteria

We use two criteria to check for FTSs in solutions of the 3D-axisymmetric IMHD equations (5): (a) the Caflisch–Klapper–Steele (CKS) criterion and (b) the analyticity-strip method [37]. We discuss the details below:

(a) *Caflisch–Klapper–Steele (CKS) criterion.* The Beale–Kato–Majda (BKM) criterion is regularly employed to look for FTSs for the 3D Euler equations [38]. It was generalized to ideal MHD flows by Caflisch, Klapper, and Steele [25] as follows:

A solution of the 3D IMHD equations remains smooth in the time interval $[0, T_*]$ *provided that*

$$\int_0^{T_*} (||\boldsymbol{\omega}(.,t)||_\infty + ||\boldsymbol{j}(.,t)||_\infty)\, dt < \infty. \tag{13}$$

For our spectral simulations, we define the global maximum $||\boldsymbol{\omega}(.,t)||_\infty$ (resp. $||\boldsymbol{j}(.,t)||_\infty$) as the maximal value of $\boldsymbol{\omega}(.,t)$ (resp. $\boldsymbol{j}(.,t)$) on the computational grid $\mathbf{X}_{N,M}$. In order to use this criterion effectively, we must capture singular structures accurately, e.g., by using an adaptive-meshing scheme (see, e.g., Refs. [30,39,40]). For our fixed-grid Fourier–Chebyshev pseudospectral scheme, we employ the analyticity-strip method for it requires the spectral approximations of the fields; these are readily available to us from our DNS.

(b) *Analyticity-strip method.* This method was developed in Ref. [37] for tracking complex-space singularities when Fourier pseudospectral schemes are used [21,32,37,41–46]. At a given instant of time t, the real-space solution $\boldsymbol{u}(x,t)$, of the PDE, can be analytically continued to complex-space variables $\mathfrak{z} = x + iy$, inside the analyticity strip $|y| < \delta(t)$. If at this time the complex singularity nearest to the real axis $\Re(x)$ is present at $\mathfrak{z}_* = x_* + i\delta$, then the Fourier spectrum of the velocity field $\hat{u}(k,t)$ behaves as

$$|\hat{u}(k,t)| \sim |k|^{-n(t)} e^{-k\delta(t)} e^i k x_*(t), \tag{14}$$

for large k. Here, μ is the exponent of the singularity and $n = \mu + 1$. The presence of multiple competing singularities close to $\Re(x)$ gives rise to oscillatory behavior in the large-k regime. In Ref. [32] we have extended the application of this method to pseudospectral studies in bounded domains, where we use Chebyshev discretization in the bounded r direction. Here, we employ our analyticity-strip method [32] to analyze the Fourier–Chebyshev spectra of the velocity and magnetic fields obtained from our DNS of the 3D-axisymmetric IMHD model (5). For our analysis, we define the Fourier–Chebyshev spectra $\mathcal{S}_V(r,k,t)$, $\mathcal{S}_B(r,k,t)$, and $\mathcal{S}_T(r,k,t)$ for the fluid kinetic energy, the magnetic energy, and the total energy $\mathcal{S}_T(r,k,t)$, respectively, as follows:

$$\mathcal{S}_V(r,k,t) := \frac{g(k)}{2N_z}(|\hat{u}^\theta|^2 + |\hat{u}^r|^2 + |\hat{u}^z|^2)\,; \tag{15a}$$

$$\mathcal{S}_B(r,k,t) := \frac{g(k)}{2N_z}(|\hat{b}^\theta|^2 + |\hat{b}^r|^2 + |\hat{b}^z|^2)\,; \tag{15b}$$

$$\mathcal{S}_T(r,k,t) := \frac{1}{2}(\mathcal{S}_V + \mathcal{S}_B)\,; \tag{15c}$$

where $g(k=0)=1$ and $g(k>0)=2$. At a given time t and radial coordinate r, we perform the nonlinear fit of the total energy spectrum $\mathcal{S}_T(r,k,t)$ using the form given in Eq. (14); we can then obtain $\delta(r,t)$ from the slope of the exponential tail in the large-k regime. If at some time t_*, $\delta \to 0$, then the nearest complex singularity hits the real axis, at this time, and the flow develops an FTS in physical space.

Any practical implementation of a pseudospectral DNS has a finite spatial resolution, so the extraction of δ can only be accurate up until the time at which the spectral approximation is relatively free from errors [47]; beyond this time spectral convergence is lost, so we stop our analysis. For the 3DAE [32] and for the 3D-axisymmetric IMHD flows that we discuss here, we see the emergence of localized oscillatory structures, called *tygers* [48], around this time; at later times the energy spectra show signs of thermalization [32,49,50].

B. Conserved quantities

The 3D IMHD equations (1) have three quadratic invariants; these are the total (kinetic + magnetic) energy E_T, magnetic helicity H_M, and the cross helicity H_C. For the 3D-axisymmetric system in Eq. (5), these are given below:

$$E_T = E_V + E_B = \frac{1}{2}\int_0^1\int_0^L |\boldsymbol{u}|^2 + |\boldsymbol{b}|^2\, r dr dz\,; \tag{16a}$$

$$H_M = \int_0^1\int_0^L \boldsymbol{\phi}\cdot\boldsymbol{b}\, r dr dz\,; \tag{16b}$$

$$H_C = \int_0^1\int_0^L \boldsymbol{u}\cdot\boldsymbol{b}\, r dr dz. \tag{16c}$$

In Fig. F1 in Supplemental Material [51] we plot vs time t the numerical conservation of the invariants of Eq. (16) achieved using our Fourier–Chebyshev pseudospectral DNS for different values of $\mathcal{C}$ specified in the legend. In panel (a) we plot the percentage relative error in total energy $\delta E_T\%$ with respect to t; thus, total energy is conserved with an accuracy of $10^{-6}\%$ for early times, until $t \sim 3\times10^{-3}$. The accuracy is gradually lost as the system nears the potential FTS. In panel (b) we plot the magnetic helicity H_M in Eq. (16b) and in panel (c) the cross helicity H_C in Eq. (16c) with time t. We observe that conservation of magnetic helicity is extremely good; however, the numerical conservation of cross helicity deteriorates for $t > 1\times10^{-3}$. This can be explained by looking at the fields which inform these quantities. The cross helicity $\boldsymbol{u}\cdot\boldsymbol{b}$ involves alignment between $\boldsymbol{u}$ and $\boldsymbol{b}$ which are both evolved independently in the numerical scheme; the errors are thus sensitive to the numerical errors *both* in $\boldsymbol{u}$ and $\boldsymbol{b}$. This is in contrast to the magnetic helicity $\boldsymbol{\phi}\cdot\boldsymbol{b}$, wherein the magnetic vector potential $\boldsymbol{\phi}$ is derived from the magnetic fields; this means that the error in magnetic helicity is sensitive only to those in the magnetic fields. The regularization of the ϕ^θ while inverting the Poisson problem (6b) as well as the inverse cascade of magnetic helicity can furthermore control the errors as the system approaches FTS when the spectral errors accumulate at the high-k modes.

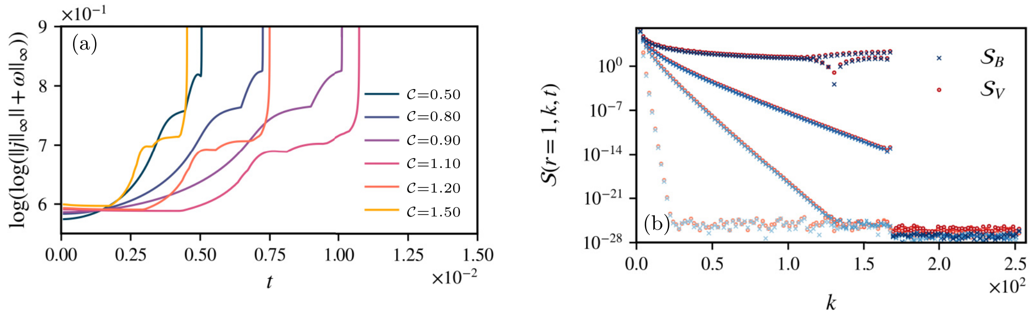

FIG. 1. (a) Plot vs t of the CKS criterion $\log(\log(||\boldsymbol{j}||_\infty + ||\boldsymbol{\omega}||_\infty))$ for different values of $\mathcal{C}$ given in the legend; here log base is 10. We see rapid growth of the CKS integrand in time, which occurs earlier for values of $\mathcal{C}$ far from $\mathcal{C} = 1$. (b) Semilog plots vs k of the Fourier spectra (see text) $\mathcal{S}_V(r = 1, k, t)$ (red) and $\mathcal{S}_B(r = 1, k, t)$ (blue) at the wall (at $r = 1$) for four different times $t = \{0.0009, 0.0034, 0.0041, 0.0062\}$. For early times these spectra (shown in faded colors) have exponential tails, with large negative slopes, so our system exhibits spectral convergence. At later times, the spectra flatten out and begin to thermalise (see text); the flow is initiated with the representative value $\mathcal{C} = 0.80$ and a resolution of $(N = 256, M = 512)$.

IV. RESULTS

We first analyze the IMHD flows evolved from the aforementioned initial data using the Caflisch–Klapper–Steele (CKS) criterion [25] in Fig. 1(a). The rapid growth of $||\boldsymbol{j}||_\infty + ||\boldsymbol{\omega}||_\infty$, the integrand in the CKS criterion (13), indicates the generation of FTSs for various values of $\mathcal{C}$. However, since we employ a fixed-grid spectral scheme, we do not rely completely on the CKS criterion for singularity detection. We now carry out a detailed study of these potential FTSs using the analyticity-strip method of Ref. [37], which is especially well suited for spectral schemes.

In order to track the nearest complex-space singularities using the analyticity-strip method, we consider the Fourier spectra $\mathcal{S}_V(r = 1, k, t)$ and $\mathcal{S}_B(r = 1, k, t)$ of the velocity and magnetic fields computed at the wall ($r = 1$), where we expect the potential FTS to precipitate, in Fig. 1(b). At large k the spectra exhibit exponentially decaying tails, so we use the asymptotic relation (14) to extract the slope $\delta_T(t)$ of the of the semilog plot in Fig. 1(b), which yields our estimate for the distance of the nearest complex singularity from the real line, at time t [52]. As time progresses, we find that $\delta_T \to 0$, i.e., the complex singularity approaches the real line, and a potential FTS develops.

Clearly the rate of decay of $\delta_T(t)$ depends on $\mathcal{C}$. In Fig. 2(a) we present log-log plots of $\delta_T(t)$ vs t; the data from our numerical simulations are shown by filled circles; and the linear regimes in these plots are consistent with the power-law forms $\delta_T(t) \sim |t - t^*(\mathcal{C})|^{\gamma(\mathcal{C})}$, which we show via solid lines. These plots provide strong evidence for FTSs in the 3D-axisymmetric IMHD model for the flows that we initialize with $\mathcal{C} \neq 1$. We display the $\mathcal{C}$ dependence of the singularity time $t^*(\mathcal{C})$ in Fig. 2(b) [53]. The case $\mathcal{C} = 1$ is special because the kinetic and magnetic terms on the RHS of Eqs. (5) cancel each other, so the solution remains stationary and there is no singularity; $t_*(\mathcal{C})$ decreases as $\mathcal{C}$ moves away from $\mathcal{C} = 1$. We plot the variation of the exponent γ with $\mathcal{C}$ in Fig. F3 in Supplemental Material [51]. We see that γ is approximately the same as we move away from $\mathcal{C} = 1$. Here we mention, for comparison, that $\gamma = 2.6 \pm 0.5$ was reported by us in Ref. [32] for the 3D-axisymmetric Euler equation; this corresponds to case for which $\mathcal{C} = 0$.

Here, we note that there are a finite number of Fourier–Chebyshev modes in any practical numerical simulation, so there is energy backflow from high-k modes, near the dealiasing cutoff K_G, and our Galerkin-truncated system moves toward thermalization [48,50], which is reflected in the flattening of $\mathcal{S}_V(r = 1, k, t)$ and $\mathcal{S}_B(r = 1, k, t)$ in Fig. 1(b) at late times t. In physical space this leads to the emergence of localized, tyger-type oscillatory structures in the kinetic and magnetic fields. Here, we note that our work reports the first observation of tyger-type resonances in MHD fluids (see [32,48,54] for other models). These structures are generated as a result of the resonant

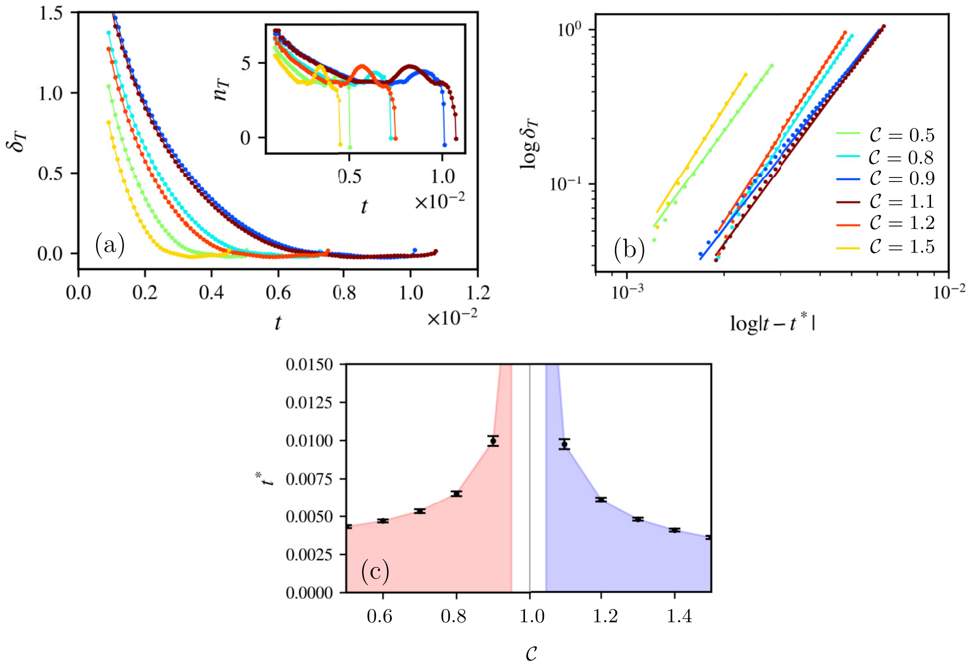

FIG. 2. Plots vs t of (a) the analyticity-strip width δ_T (and n_T in the inset) obtained by performing the nonlinear fit (14) of the total energy Fourier spectrum at the wall ($r = 1$) for flows initiated with different choices of $\mathcal{C}$ in the initial data. (b) Log-log plot vs $|t - t^*|$ of $\log \delta_T$ and the corresponding power-law fit $\delta_T \sim |t - t^*(\mathcal{C})|^{\gamma(\mathcal{C})}$ for flows initiated with different choices of $\mathcal{C}$ in the initial data. (c) Plot vs $\mathcal{C}$ of the estimate for the time of singularity $t^*(\mathcal{C})$ that we obtain from the power-law fit of $\delta_T(t)$ from (a); we use ($N = 256$, $M = 512$). See Fig. F3 in Supplemental Material for the $\mathcal{C}$ dependence of the exponent γ [51].

wave-particle interaction between the truncation wave and the fluid particles moving with its phase velocity in the spectrally discretized solution [48]. The emergence of tygers signals the loss of spectral convergence and the simultaneous onset of thermalization in these Hamiltonian systems. In this context our results have implications for the general problem of thermalization in spectrally truncated ideal hydrodynamical systems [32,48–50,55].

To understand the development of the singularity in physical space, we now examine the streamlines and secondary flows of the velocity and magnetic fields, for two illustrative values of $\mathcal{C} = 0.8$ and $\mathcal{C} = 1.2$; henceforth, we refer to the resulting flows as flow A and flow B, respectively. The estimates for the time of singularity are $t_* = 6.5 \times 10^{-3} \pm 1.6 \times 10^{-4}$ for flow A and $t_* = 6.1 \times 10^{-3} \pm 1.2 \times 10^{-4}$ for flow B. The observations that we make for flow A (flow B) hold true for flows initialized with other choices for $\mathcal{C}$, with $\mathcal{C} < 1$ ($\mathcal{C} > 1$).

Profile at the wall. In flow A the velocity fields are initially stronger than their magnetic counterparts. In Fig. 3(a) we observe that at early times ($t = 9 \times 10^{-4}$), u^θ has a nearly sinusoidal profile at the wall, which develops into a square profile at later times ($t = 6.1 \times 10^{-3}$). This in turn results in the intensification of shear at the meridional plane ($r = 1$, $z = L/2$), and tygers appear near $z = \{L/4, 3L/4\}$ at this time (for similar plots of other fields, see Fig. F2 in Supplemental Material [51]).

In flow B [$\mathcal{C} = 1.2$] the magnetic field is initially stronger than the velocity field. In Fig. 3(b) the plots of $u^\theta(z)$ at the wall ($r = 1$), for various representative times, show that the initial sinusoidal profile of $u^\theta(r = 1, z)$ (yellow line) evolves into a tentlike profile (pink line) at intermediate times, losing differentiability at $z = L/4,\ 3L/4$. At later times [e.g., $t \simeq 6.1 \times 10^{-3}$], this is damped (blue line) as the flow decelerates along the wall, and we see the development of cusps in $u^\theta(r = 1, z$ at

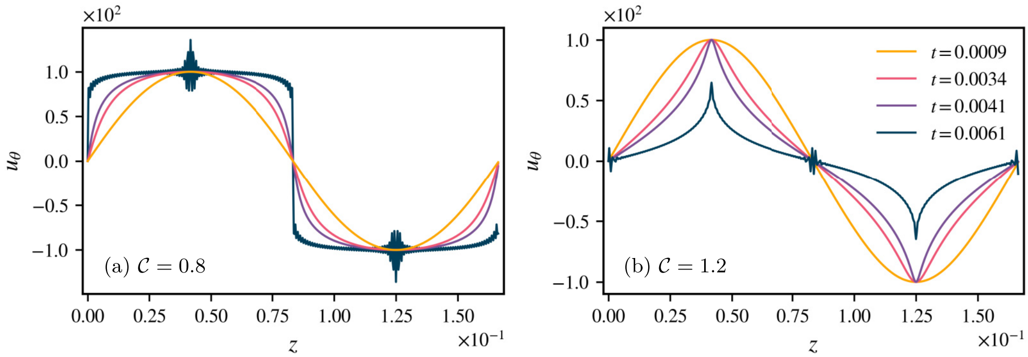

FIG. 3. Plots vs z of the swirl velocity $u^\theta(r = 1, z)$ superposed for various times t listed in the legend, for flows initiated with (a) $\mathcal{C} = 0.80$ and (b) $\mathcal{C} = 1.20$. Here, we use a resolution of ($N_r = 256, N_z = 512$). At later times we see the development of localized oscillatory structures (tygers) in these fields. See Supplemental Material [51] for similar plots of b^θ.

$z = \{L/4, 3L/4\}$, which are distinctly different from the square-type profile in Fig. 3(a) for flow A; tygers appear too, but away from the positions of the cusps.

Secondary flows and streamlines. In order to understand the spatiotemporal evolution of u^θ at the wall described above, we now study the secondary flows in the $r - z$ plane. We present, for flow A, (i) plots of the streamlines for the velocity field $\boldsymbol{u}$, in 3D [Fig. 4(a)] and (ii) plots of the streamlines of the secondary flow in the $r - z$ plane [blue-green solid lines in Fig. 4(b)], superposed on the heat-map of u^θ for time $t = 0.0055$. The secondary flow consists of the fluid rotating in the $r - z$ plane, within convection-type cells, along the wall. The direction of rotation of the cells is

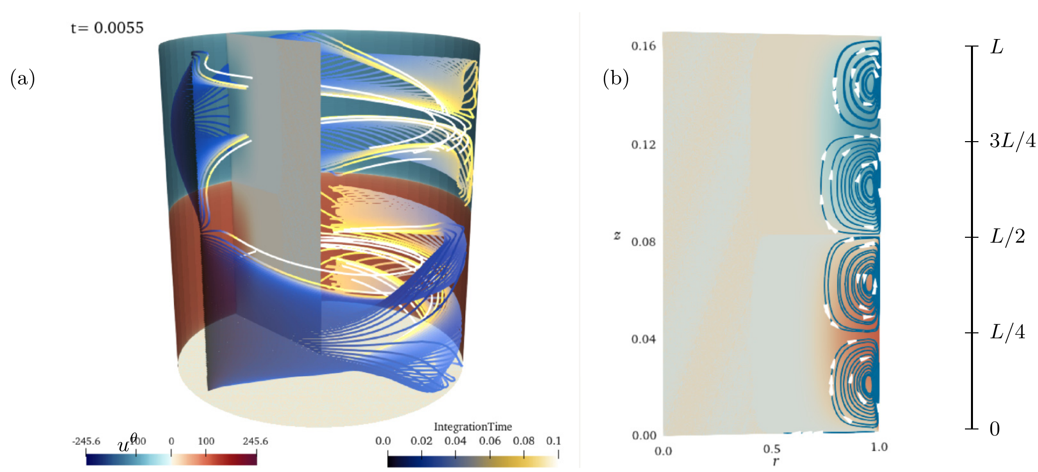

FIG. 4. Flow A: (a) Plot of the streamlines of the axisymmetric velocity field $\boldsymbol{u}$ seeded from a straight line (shown on the left side, inside cylinder) at time $t = 0.0055$. We plot the heat-map of $u^\theta(r, z)$ on the back-face of the cylinder. At early integration times, the streamlines (blue) are pushed outward toward the wall by the secondary flows; at later integration times, they flatten on the wall, leading to the square-type profile of $u^\theta(r = 1, z)$ shown in Fig. 3(a). (b) Plots of streamlines (blue-green) of the secondary flows driven by $\boldsymbol{u}$ in the $r - z$ plane, superposed over the heat-map of u^θ at the same time $t = 0.0055$. We initiate the flow with $\mathcal{C} = 0.80$ and use ($N = 256$, $M = 512$) for this run.

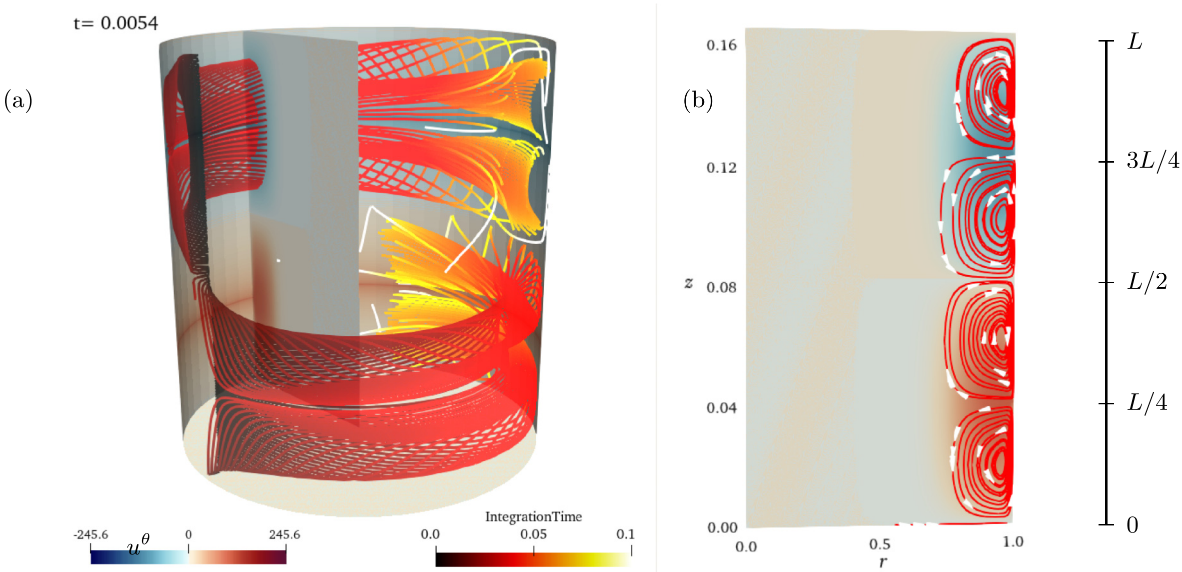

FIG. 5. Flow B: (a) Plot of the streamlines of the axisymmetric velocity field $\boldsymbol{u}$ seeded from a straight line (shown on the left side, inside cylinder) at time $t = 0.0054$. We plot the heat-map of $u^\theta(r, z)$ on the back-face of the cylinder. The streamlines (red) are twisted and pulled inward by the secondary flows at $z = \{L/4, 3L/4\}$, close to the singularity time $t^*(\mathcal{C})$, and this leads to the cusplike profile of $u^\theta(r = 1, z)$ shown in Fig. 3(b). (b) Plots of streamlines (red) of the secondary flows driven by $\boldsymbol{u}$ in the $r - z$ plane, superposed over the heat map of u^θ at the same time $t = 0.0054$. We initiate the flow with $\mathcal{C} = 1.20$ and use ($N = 256$, $M = 512$) for this run.

such that the fluid is driven away from $z = \{L/4, 3L/4\}$ *along the wall;* thereby, the initial maxima of $u^\theta(r = 1)$ at these locations are similarly advected outward by u^z.

In Fig. 4(a) we see that the streamlines, which have been started out along a straight line (blue), move into (out of) the plane given the negative (positive) sign of u^θ in the upper (lower) half of the cylinder. They bulge outward toward the wall, because of the influence of the secondary flows, near $z = \{L/4, 3L/4\}$. At later integration times, the streamlines (yellow), which have started from near $z = \{L/4, 3L/4\}$, fan out at the wall; this is nothing but the advection of u^θ outward from $z = \{L/4, 3L/4\}$. For this time we show the heat-map of u^θ on the back- face of the cylinder (colorbar of u^θ), from which we can deduce the square profile of $u^\theta(r = 1, z)$ at late times [cf. Fig. 3(a)]; this leads gradually to uniform blue-green (orange) coloring of the heat-map in the upper (lower) half of the cylinder.

For flows initiated with $\mathcal{C} < 1$, real-space dynamics of the velocity field $\boldsymbol{u}$ closely follow the dynamics summarized above for flow A with $\mathcal{C} = 0.8$; however, as $\mathcal{C}$ decreases, $t_*(\mathcal{C})$ decreases [Fig. 2(b)]. It is important to note that the mechanism that we report here, for flow A, is akin to that seen for the potentially singular flow in the 3D-axisymmetric wall-bounded Euler equation [30–32] ($\mathcal{C} = 0$ here). Furthermore, the spatiotemporal evolution of the magnetic field $\boldsymbol{b}$ is similar to that of $\boldsymbol{u}$; in particular, we see the development of a square profile of b^θ at the wall (see Fig. F2 in Supplemental Material [37]).

For flow B we now discuss the secondary flows in the $r - z$ plane that lead to the formation of the tentlike profile of $u_\theta(r = 1, z)$ in Fig. 3. As for flow A, we visualize (i) the streamlines for the axisymmetric velocity field $\boldsymbol{u}$ [Fig. 5(a)] and (ii) the streamlines of the secondary flow in the $r - z$ plane [Fig. 5(b)] at time $t = 0.0054$.

The red streamlines [Fig. 5(b)] of the secondary flow in the $r - z$ plane, superposed on the heat-map of u^θ, show rotating cells of fluid, similar to those for flow A [Fig. 4(b)] but with the opposite

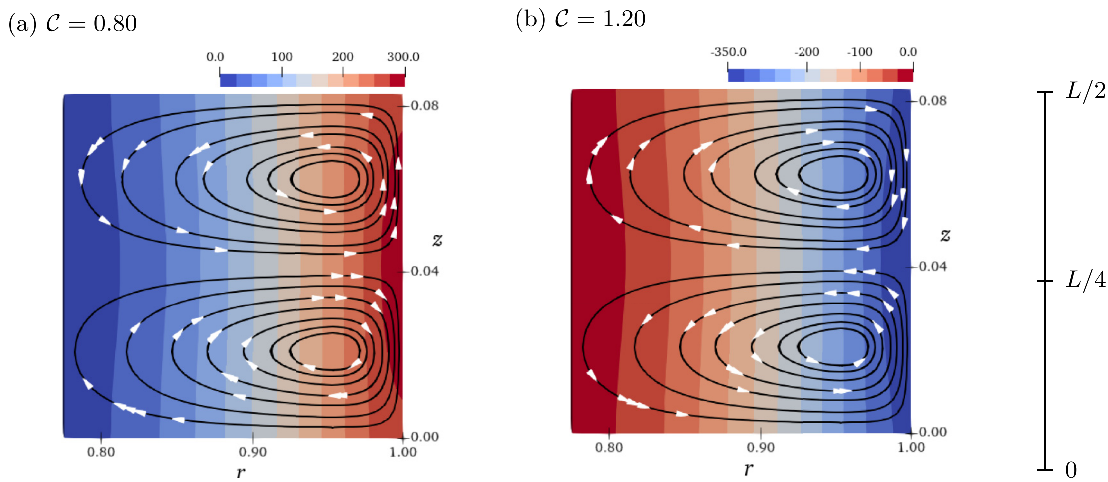

FIG. 6. Streamline plots of the secondary flows in the $r - z$ half-plane superposed on the heat-map of the effective pressure P for (a) flow A $\mathcal{C} = 0.80$ and (b) flow B $\mathcal{C} = 1.20$ at time $t = 1 \times 10^{-4}$. We see that the flow moves outward from the pressure maximum at $(r = 1, z = L/4)$ along the wall for flow A. For flow B the flow moves into the pressure minimum at the same point. See Fig. F4 in Supplemental Material for the pressure field at later times [51].

direction of rotation. Here, the secondary flow is such that the fluid is driven *toward* $z = \{L/4, 3L/4\}$ *on the wall*. This leads to the pinching of the initially sinusoidal profile of u^θ, because of its advection by u^z, which now points inward at $z = \{L/4, 3L/4\}$ in these cells.

The deceleration of the flow along the wall can be seen clearly in the streamline plot [Fig. 5(a)], which is seeded as in Fig. 4(a). Here, flow B is distinctly different from flow A: the sheet formed by the streamlines in each half of the cylinder folds in on itself at $z = \{L/4, 3L/4\}$ (dark red) because of the advection of the slower-moving fluid inward, at these points, by the secondary flow. Thus, at later integration times (yellow) the streamlines seeded near $z = \{0, L/2\}$ move toward $z = L/4$ in the upper half of the cylinder; we see similar dynamics in the lower half, where the fluid rotates with positive swirl velocity. Correspondingly, the heat-map of u^θ, shown on the back face of the cylinder, displays an intensification of velocity solely at $z = \{L/4, 3L/4\}$ [in contrast with the heat-map of Fig. 4(a), where the flow is accelerated everywhere along the wall]. Thus, our examination of secondary flows elucidates the magnetic-field-induced suppression of the swirl velocity at the wall an the formation of cusps in flow B.

Role of pressure. We now demonstrate that the pressure plays a crucial role in establishing the secondary flows discussed above, which in turn lead to the formation of FTS in the IMHD flows. We obtain the pressure from the divergence of Eq. (1a) that yields the Poisson-type equation (11). For our IMHD flows, we define the effective pressure $P = p + \frac{1}{2}|\boldsymbol{b}|^2$, which we compute for flow A and flow B using the Fourier–Chebyshev Tau Poisson solver developed by us [32].

In Figs. 6(a) and 6(b) we show, respectively, the heat-maps of $P(r, z)$, computed at the early time $t = 10^{-4}$ close to the wall, in the lower half ($r \in [0.7, 1]$, $z \in [0, 1/12]$) of the cylinder, for (a) flow A and (b) flow B; we superpose the streamlines of the corresponding secondary flows.

From Fig. 6(a) we can deduce that for flow A, the pressure is lowest at the axis and it increases as $r \to 1$; along the wall $r = 1$, a local pressure maximum develops at $z = L/4$. As a result, we see that the fluid moves *along* the pressure gradient on the wall, i.e., it moves outward from the pressure maximum at $z = L/4$, in the z direction; and, in the r direction, it moves away from the wall at $z = \{0, L/2\}$. At $z = L/4$, the fluid is forced to move against the local pressure gradient by virtue of incompressibility, thereby enforcing the direction of rotation of the fluid in the cells. Thus, the secondary flow rotates anticlockwise for $z > L/4$ and clockwise for $z < L/4$.

In contrast, for flow B [Fig. 6(b)], the effective pressure P is lower at the wall and increases as $r \to 0$; now, there is a local minimum of P at $z = L/4$ [cf. the maximum of P for flow A in Fig. 6(a)]. As a result, the fluid moves toward $z = L/4$ along the wall, and then it moves outward radially, toward the wall at $z = \{0, L/2\}$.

We can relate the pressure field, which develops at initial times, to the initial data by considering the radial-pressure balance at $r = 1$ (on the wall), as shown in Eq. (17). In order to obtain the radial force balance, we consider the r component of the 3DA-IMHD equations (5) and we assume that the flow is instantaneously stationary right before initialization; thus, the LHS vanishes and we get, along $\hat{e}_r$, at $r = 1$ and $t = 0$:

$$\underbrace{-\partial_r\left(p + \frac{(b^\theta)^2}{2}\right)}_{F_P} + \underbrace{\frac{(u^\theta)^2 - (b^\theta)^2}{r}}_{F_R} = 0. \tag{17}$$

We find that the gradient of $P \equiv [p + \frac{1}{2}(b^\theta)^2]$ has to balance the centrifugal force $[(u^\theta)^2/r$ that points outward along $\hat{e}_r]$, *minus* the curvature forces because of the tension of the magnetic field lines $[(b^\theta)^2/r$, inward along $\hat{e}_r]$, at the wall. For flow A, $\mathcal{C} = 0.8$ and $b_0^\theta(r, z) = 0.8\, u_0^\theta(r, z)$; thus, the centrifugal force is dominant, giving a resultant force F_R that points outward along $\hat{e}_r$. In order to achieve force balance, P is set up in a way such that its radial gradient points outward along $\hat{e}_r$ to balance the resultant force above [note the sign in F_P in Eq. (17)]. This is verified by the heat-map of P shown in Fig. 6(a), with P increasing as $r \to 1$; the pressure maximum occurs at $z \to L/4$ as $(u^\theta)^2 - (b^\theta)^2$ and assumes its largest value here.

By contrast, for flow B where $\mathcal{C} = 1.20$, the magnetic-tension forces dominate over the centripetal forces, and the resultant force F_R points radially inward. The pressure field P is now such that its radial gradient points inward. This is seen in Fig. 6(b), where the pressure decreases as $r \to 1$ and the local minimum occurs at $z = L/4$, where the F_R attains its largest value.

In Figs. F4(a) and F4(b) of Supplemental Material [51], we show the evolution of the pressure field $P(r, z)$, at time $t = 4.9 \times 10^{-3}$ closer to the time of singularity for (a) flow A and (b) flow B; we superpose the streamlines of the corresponding secondary flows. A detailed analysis of the role played by pressure in sustaining the driving mechanism for the singularity can be carried out along the lines of [31]; we will discuss these points in future work.

V. CONCLUSIONS

In conclusion, the global regularity of solutions of 3D hydrodynamical PDEs, such as the 3D IMHD equations, continues to challenge physicists, fluid dynamicists, and mathematicians. Numerical studies play an important role in the quest for FTSs in such PDEs. We have taken the first crucial step that is required for uncovering FTSs in the 3D IMHD equations: In particular, we have presented compelling numerical evidence for the development of (potential) finite-time singularities in these equations in a wall-bounded axisymmetric domain. Furthermore, we have obtained deep insights into these FTSs by examining secondary flows and their dependence on the effective pressure P at initial times.

Our study brings out clearly the importance of emergent secondary flows, arising from differential rotation, and the role played by the effective pressure P in their development. Had the system been a viscous and resistive *MHD fluid*, then the boundaries would have led to *Ekman pumping*, well studied in the contexts of magnetic stirring of liquid metals [18,56]. In the potential FTS flows that we consider [57], the differential rotation arises by virtue of the initial data.

The singular solutions we uncover are of two types—either they display developing *discontinuities* or *cusps*—depending on the relative magnitudes of the kinetic and magnetic fields at the initial time; the cusp-type singularities have not been anticipated in the types of PDEs we study. Our findings demonstrate the role played by the magnetic field in suppressing and changing the type of singularity that is observed in this model. Both these types of singularities will be of relevance and interest to plasma-physicists, fluid-dynamicists, and mathematicians. In particular, the potential FTSs we find should aid in the development of rigorous proofs for the global regularity (or lack thereof) of solutions to the 3D IMHD PDEs, with the initial data we have proposed.

ACKNOWLEDGMENTS

We thank T. Hertel, N. Besse, J. K. Alageshan, M. Brachet, and T. Matsumoto for useful discussions; and we thank the Anusandhan National Research Foundation (ANRF), the Science and Engineering Research Board (SERB), and the National Supercomputing Mission (NSM), India, for support, and the Supercomputer Education and Research Centre (IISc), for computational resources.

DATA AVAILABILITY

There are no publicly available research data or software supporting this manuscript. Requests for further information or data should be sent to the authors.

---

[1] C. R. Doering and J. D. Gibbon, *Applied Analysis of the Navier-Stokes Equations* (Cambridge University Press, Cambridge, UK, 1995).

[2] G. P. Galdi, An introduction to the Navier-Stokes initial-boundary value problem, in *Fundamental Directions in Mathematical Fluid Mechanics* (Springer, New York, 2000), pp. 1–70.

[3] C. Foias, O. Manley, R. Rosa, and R. Temam, *Navier-Stokes Equations and Turbulence* (Cambridge University Press, Cambridge, UK, 2001), Vol. 83.

[4] J. C. Robinson, J. L. Rodrigo, and W. Sadowski, *The Three-Dimensional Navier–Stokes Equations: Classical Theory* (Cambridge University Press, Cambridge, UK, 2016), Vol. 157.

[5] P. G. Lemarié-Rieusset, *The Navier-Stokes Problem in the 21st Century* (Chapman and Hall/CRC, London, 2018).

[6] J. C. Robinson, The Navier–Stokes regularity problem, Philos. Trans. R. Soc. Lond. Ser. A **378**, 20190526 (2020).

[7] J. A. Carlson, A. Jaffe, and A. Wiles, *The Millennium Prize Problems* (American Mathematical Society, Providence, RI, 2006).

[8] To quote from Ref. [7]: “Show that the Navier–Stokes equations on Euclidean 3-space have a unique, smooth, finite energy solution for all time greater than or equal to zero, given smooth, divergence-free, initial conditions which “decay rapidly at large distances. Alternatively, show that there is no such solution.”

[9] V. I. Yudovich, Non-stationary flow of an ideal incompressible liquid, USSR Comput. Math. Math. Phys. **3**, 1407 (1963).

[10] L. Onsager, Statistical hydrodynamics, Nuovo Cim. **6**, 279 (1949).

[11] G. L. Eyink and K. R. Sreenivasan, Onsager and the theory of hydrodynamic turbulence, Rev. Mod. Phys. **78**, 87 (2006).

[12] M. Paicu and N. Zhu, Global regularity for the 2D MHD and tropical climate model with horizontal dissipation, J. Nonlinear Sci. **31**, 99 (2021).

[13] D. Biskamp, *Magnetohydrodynamic Turbulence* (Cambridge University Press, Cambridge, England, 2003).

[14] A. R. Choudhuri, *The Physics of Fluids and Plasmas: An Introduction for Astrophysicists* (Cambridge University Press, Cambridge, England, 1998).

[15] J. H. Goedbloed and S. Poedts, *Principles of Magnetohydrodynamics: With Applications to Laboratory and Astrophysical Plasmas* (Cambridge University Press, England, 2004).

[16] J. P. Freidberg, *Ideal MHD* (Cambridge University Press, Cambridge, England, 2014).

[17] S. Galtier, *Introduction to Modern Magnetohydrodynamics* (Cambridge University Press, Cambridge, England, 2016).
[18] P. A. Davidson, *Introduction to Magnetohydrodynamics* (Cambridge University Press, Cambridge, England, 2017), Vol. 55.
[19] D. A. Gurnett and A. Bhattacharjee, *Introduction to Plasma Physics: With Space, Laboratory and Astrophysical Applications* (Cambridge University Press, Cambridge, England, 2017).
[20] J. P. Goedbloed, H. Goedbloed, R. Keppens, and S. Poedts, *Magnetohydrodynamics: Of Laboratory and Astrophysical Plasmas* (Cambridge University Press, Cambridge, England, 2019).
[21] M. E. Brachet, M. D. Bustamante, G. Krstulovic, P. D. Mininni, A. Pouquet, and D. Rosenberg, Ideal evolution of magnetohydrodynamic turbulence when imposing Taylor-Green symmetries, Phys. Rev. E **87**, 013110 (2013).
[22] V. Dallas and A. Alexakis, The signature of initial conditions on magnetohydrodynamic turbulence, Astrophys. J. **788**, L36 (2014).
[23] P. D. Mininni and A. Pouquet, Finite dissipation and intermittency in magnetohydrodynamics, Phys. Rev. E **80**, 025401(R) (2009).
[24] M. F. Linkmann, A. Berera, W. D. McComb, and M. E. McKay, Nonuniversality and finite dissipation in decaying magnetohydrodynamic turbulence, Phys. Rev. Lett. **114**, 235001 (2015).
[25] R. E. Caflisch, I. Klapper, and G. Steele, Remarks on singularities, dimension and energy dissipation for ideal hydrodynamics and MHD, Commun. Math. Phys. **184**, 443 (1997).
[26] J. Gibbon, The three-dimensional Euler equations: How much do we know? Physica D **237**, 1894 (2008).
[27] T. Y. Hou, Blow-up or no blow-up? A unified computational and analytic approach to 3D incompressible Euler and Navier–Stokes equations, Acta Numer. **18**, 277 (2009).
[28] R. M. Kerr and A. Brandenburg, Evidence for a singularity in ideal magnetohydrodynamics: Implications for fast reconnection, Phys. Rev. Lett. **83**, 1155 (1999).
[29] R. Grauer and C. Marliani, Current-sheet formation in 3D ideal incompressible magnetohydrodynamics, Phys. Rev. Lett. **84**, 4850 (2000).
[30] G. Luo and T. Y. Hou, Potentially singular solutions of the 3D axisymmetric Euler equations, Proc. Natl. Acad. Sci. USA **111**, 12968 (2014).
[31] D. Barkley, A fluid mechanic's analysis of the teacup singularity, Proc. R. Soc. Lond. Ser. A **476** 20200348 (2020).
[32] S. S. V. Kolluru, P. Sharma, and R. Pandit, Insights from a pseudospectral study of a potentially singular solution of the three-dimensional axisymmetric incompressible Euler equation, Phys. Rev. E **105**, 065107 (2022).
[33] T. Hertel, N. Besse, and U. Frisch, The Cauchy-Lagrange method for 3D-axisymmetric wall-bounded and potentially singular incompressible Euler flows, J. Comput. Phys. **449**, 110758 (2022).
[34] Cusp singularities have been at interfaces between different fluids, as discussed, e.g., in Refs. [58,59].
[35] T. Y. Hou and R. Li, Blowup or no blowup? The interplay between theory and numerics, Physica D **237**, 1937 (2008).
[36] M. Uhlmann, The Need for De-Aliasing in a Chebyshev Pseudo-Spectral Method, Potsdam Institut fur Klimafolgenforschung, Potsdam, Germany, 2000.
[37] C. Sulem, P.-L. Sulem, and H. Frisch, Tracing complex singularities with spectral methods, J. Comput. Phys. **50**, 138 (1983).
[38] J. T. Beale, T. Kato, and A. Majda, Remarks on the breakdown of smooth solutions for the 3D Euler equations, Commun. Math. Phys. **94**, 61 (1984).
[39] R. Grauer and C. Marliani, Geometry of singular structures in magnetohydrodynamic flows, Phys. Plasmas **5**, 2544 (1998).
[40] R. Grauer, C. Marliani, and K. Germaschewski, Adaptive mesh refinement for singular solutions of the incompressible Euler equations, Phys. Rev. Lett. **80**, 4177 (1998).
[41] M. E. Brachet, D. I. Meiron, S. A. Orszag, B. Nickel, R. H. Morf, and U. Frisch, Small-scale structure of the Taylor–Green vortex, J. Fluid Mech. **130**, 411 (1983).
[42] S. Kida, Study of complex singularities by filtered spectral method, J. Phys. Soc. Jpn. **55**, 1542 (1986).

[43] M. Brachet, M. Meneguzzi, A. Vincent, H. Politano, and P. Sulem, Numerical evidence of smooth self-similar dynamics and possibility of subsequent collapse for three-dimensional ideal flows, Phys. Fluids **4**, 2845 (1992).

[44] U. Frisch, T. Matsumoto, and J. Bec, Singularities of Euler flow? Not out of the blue! J. Stat. Phys. **113**, 761 (2003).

[45] M. D. Bustamante and M. Brachet, Interplay between the Beale-Kato-Majda theorem and the analyticity-strip method to investigate numerically the incompressible Euler singularity problem, Phys. Rev. E **86**, 066302 (2012).

[46] C. Cichowlas and M. Brachet, Evolution of complex singularities in Kida–Pelz and Taylor–Green inviscid flows, Fluid Dyn. Res. **36**, 239 (2005).

[47] S. S. V. Kolluru, N. Besse, and R. Pandit, Novel spectral methods for shock capturing and the removal of tygers in computational fluid dynamics, J. Comput. Phys. **519**, 113446 (2024).

[48] S. S. Ray, U. Frisch, S. Nazarenko, and T. Matsumoto, Resonance phenomenon for the Galerkin-truncated Burgers and Euler equations, Phys. Rev. E **84**, 016301 (2011).

[49] C. Cichowlas, P. Bonaïti, F. Debbasch, and M. Brachet, Effective dissipation and turbulence in spectrally truncated Euler flows, Phys. Rev. Lett. **95**, 264502 (2005).

[50] P. C. Di Leoni, P. D. Mininni, and M. E. Brachet, Dynamics of partially thermalized solutions of the Burgers equation, Phys. Rev. Fluids **3**, 014603 (2018).

[51] See Supplemental Material at http://link.aps.org/supplemental/10.1103/l645-3ljm for for additional figures.

[52] We have used the `LMFIT` package from python to perform the nonlinear fitting.

[53] From the fit window, we exclude the range for which $\delta < \Delta z$, where Δz is the smallest grid spacing in $\mathbf{X}_{256,512}$.

[54] S. D. Murugan and S. S. Ray, Genesis of thermalization in the three-dimensional, incompressible, Galerkin-truncated Euler equation, Phys. Rev. Fluids **8**, 084605 (2023).

[55] S. D. Murugan, U. Frisch, S. Nazarenko, N. Besse, and S. S. Ray, Suppressing thermalization and constructing weak solutions in truncated inviscid equations of hydrodynamics: Lessons from the Burgers equation, Phys. Rev. Res. **2**, 033202 (2020).

[56] P. Davidson, D. Kinnear, R. Lingwood, D. Short, and X. He, The role of Ekman pumping and the dominance of swirl in confined flows driven by Lorentz forces, Eur. J. Mech. B Fluids **18**, 693 (1999).

[57] For the 3DAE, see Refs. [30–32].

[58] J.-T. Jeong and H. K. Moffatt, Free-surface cusps associated with flow at low Reynolds number, J. Fluid Mech. **241**, 1 (1992).

[59] J. Eggers, Viscous free-surface cusps: Local solution, Phys. Rev. Fluids **8**, 124001 (2023).